Light propagation in nanophotonic waveguides considering graphene's saturable absorption

D. Chatzidimitriou ◉* and E. E. Kriezis ◉

Department of Electric and Computer Engineering, Aristotle University of Thessaloniki, Thessaloniki 541 24, Greece

We study saturable absorption in graphene-comprising nanophotonic waveguides taking into account the finite relaxation time as well as the carrier diffusion due to the nonuniform, tightly confined spatial profile of the guided modes. We discuss various details of graphene SA and comment on the necessary conditions that allow for directly comparing our model with available experimental. The mathematical framework is based on the nonlinear Schrödinger equation which provides a strict framework for our analysis and is developed for two optical channels. We explore the propagation of cw, long and short pulsed signals in a silicon slot waveguide and show the importance of our model in order to capture the ultrafast dynamics of graphene and the spatial distribution of guided modes. Finally, we demonstrate how cross absorption modulation can be exploited in order to imprint data from a high power optical channel to a low power channel.

I. INTRODUCTION

Graphene has been the most systematically studied two-dimensional (2D) material with applications expanding into many diverse scientific fields [1]. Specifically in optics and photonics, graphene's linear electronic dispersion gives rise to many unique optical properties [2], with the most prominent being graphene's universal (broadband) light absorption [3]. Moreover, graphene's conductivity can be controlled through chemical doping and more importantly through dynamic electrostatic gating [4–6]. The exploration of these linear characteristics has led to the theoretical and experimental design of novel graphene-based devices [7–9]. Furthermore, it was also reported that graphene exhibits very high (comparable to silicon and silica) Kerr-like (third order) nonlinear properties [10,11]. The exact magnitude of the Kerr nonlinearity is still investigated [12–14], mainly because early experimental works focused on extracting an effective bulk nonlinear susceptibility for graphene, by artificially treating graphene as a thin uniform layer. More recent studies have shifted into identifying graphene's nonlinear surface conductivity as the appropriate quantity to correctly capture the nonlinear optical properties of 2D materials [15]. Nevertheless, many works have been published exploiting graphene's third-order nonlinear response in order to realize all optical devices [16–21].

Besides the Kerr effect, graphene is also known to exhibit low power and ultrafast saturable absorption (SA). In fact, the power threshold is lower than that of the Kerr effect and also much lower than in semiconductor-based saturable absorbers, rendering graphene SA very attractive as an alternate nonlinear effect [22–24]. In early publications graphene SA was exploited to experimentally realize passively mode-locked fiber lasers for femtosecond pulses [25,26]. Initially graphene was placed on the fiber ferrule but this technique

provided weak interaction. New approaches to increase light matter interaction include the use of multiple graphene sheets [22], graphene sheets placed on top of microfibers [27], fiber tapers embedded in graphene-polymer composite [28], folding graphene sheets around the fiber [29], and D-shaped fibers [30]. The 2D planar geometry of graphene, which makes it compatible with established integration techniques for SOI-based photonic devices and the above need for stronger nonlinear interaction has led to an increasing interest of exploring graphene SA in photonic waveguides [31–33], which could lead to on-chip mode-locked lasers and novel compact all-optical components. Last but not least, the two decisive experimental parameters regarding the SA effect, namely the saturation intensity (light intensity at which absorption is halved) and response time still show appreciable variation with reports differing by two or three orders of magnitude [24,26,34–39]. This has sparked an intense ongoing research into the ultrafast graphene SA dynamics and how they are properly modeled for nanophotonic waveguides.

In this work we propose a strict framework, based on the nonlinear Schrödinger equation (NLSE), for the macroscopic modeling of light propagation in photonic waveguides that have 2D materials with SA. This is achieved through a strict NLSE procedure by including the surface conductivity of the 2D material. The surface conductivity is dependent on the photoexcited carrier concentration, which in turn is described by a separate rate equation. We take into account both a finite carrier relaxation time and carrier diffusion in the 2D material, which becomes important in high confinement, and shed light on the conditions that allow direct comparison of our model with experimental data. The theory is eventually specialized for graphene and we discuss the graphene-specific details. The developed NLSE also takes into account the scenario of a probe and signal scenario at different frequencies which can be used to explore the cross absorption modulation between two such signals. Finally, we apply our theory into two distinct cases, cw and pulsed excitation. In the cw case we compare

─────────
*dchatzid@auth.gr

our model with other other simpler models and we extract an effective saturation intensity which takes into account the waveguide confinement and carrier diffusion. This greatly simplifies the propagation of long pulses where SA can be thought to be instantaneous. Next, we explore a short pulse excitation example where we show the asymmetric effects of the ultrafast temporal response of graphene SA. Furthermore, we also investigate the interplay between SA, linear dispersion, and the Kerr effect, which results into a solitonlike behavior. Finally, we simulate the simultaneous propagation of two different wavelengths and how SA can be used to imprint a data stream from one channel to the other.

II. GRAPHENE-SATURABLE ABSORPTION

In this section we establish a general macroscopic physical model for a 2D saturable absorber and then discuss how this is applied specifically to a graphene sheet.

A. Saturable surface current

We consider a quasimonochromatic electric field with central frequency ω_0 that interacts with a 2D saturable absorber. The notation used for the real electric field $\mathcal{E}$ is

$$\mathcal{E}(\mathbf{r}, t) = \tfrac{1}{2}[\mathbf{E}(\mathbf{r}, t)e^{-i\omega_0 t} + \text{c.c.}], \qquad (1)$$

where $\mathbf{E}(\mathbf{r}, t)$ is the complex slowly varying field envelope. The induced first-order macroscopic current density envelope $\mathbf{J}$ at ω_0 can be written in the time domain as

$$\mathbf{J} = \bar{\sigma}^{(1)}(\omega_0)\mathbf{E}, \qquad (2)$$

where $\bar{\sigma}^{(1)}(\omega_0)$ is the first-order (linear or low power) conductivity tensor, which is assumed to be constant around ω_0. In general the current density consists of both surface and bulk contributions, originating from 2D and bulk materials, respectively. Without loss of generality we can ignore bulk current densities so that we are left with just a surface current density,

$$\mathbf{J} = \mathbf{J}_s \delta_s(\mathbf{r}) = \bar{\sigma}_s^{(1)}(\omega_0)\mathbf{E}\delta_s(\mathbf{r}), \qquad (3)$$

where $\mathbf{J}_s$ is the surface current density, $\bar{\sigma}_s^{(1)}$ is the surface first-order conductivity tensor, and $\delta_s(\mathbf{r})$ is a surface Dirac function which is nonzero only on the 2D material. Note that $\bar{\sigma}_s^{(1)}$ has to be anisotropic so that there are no current components normal to the 2D surface. For example, a layer of a 2D material aligned in the zx plane would have a conductivity $\bar{\sigma}_s^{(1)}$ given by

$$\bar{\sigma}_s^{(1)} = \begin{bmatrix} \sigma_{1,xx} & 0 & \sigma_{1,xz} \\ 0 & 0 & 0 \\ \sigma_{1,zx} & 0 & \sigma_{1,zz} \end{bmatrix}, \qquad (4)$$

where $\sigma_{1,xy} = \sigma_{1,yx} = 0$ and $\sigma_{1,zy} = \sigma_{1,yz} = 0$. In the absence of strong magnetic fields, $\sigma_{1,xx} = \sigma_{1,zz} = \sigma_1$ and $\sigma_{1,xz} = \sigma_{1,zx} \approx 0$, thus we can simplify Eq. (3) as

$$\mathbf{J} = \sigma_1 \mathbf{E}_{||} \delta_s(\mathbf{r}), \qquad (5)$$

where the scalar σ_1 is the only independent value of $\bar{\sigma}_s^{(1)}(\omega_0)$ and $\mathbf{E}_{||}$ is the electric field parallel to the 2D material [40].

Saturable absorption is introduced as the saturation of the σ_1 conductivity in Eq. (5). This conductivity is usually thought as linear, i.e., the current density of Eq. (5) is a linear function of $\mathbf{E}_{||}$. Under the effects of SA though, the relation between current density and electric field becomes nonlinear since the conductivity now depends on the light intensity, which is proportional to $|\mathbf{E}_{||}|^2$. Microscopically, SA can be attributed to band filling: As the conduction band is filled by photoexcited carriers due to direct intraband transitions, the probability of further transitions is lowered and absorption is gradually saturated [41]. Thus, we assume that σ_1 is dependent on the surface carrier density N_c and write σ_1 as

$$\sigma_1(N_c) = \sigma_{\text{nsat}} + \sigma_{\text{sat}}(N_c), \qquad (6)$$

where σ_{nsat} and σ_{sat} are nonsaturable and saturable surface conductivity components, respectively. Combining Eqs. (5) and (6), the total current density is expressed as the sum of two distinct surface current densities,

$$\mathbf{J} = (\mathbf{J}_{\text{lin}} + \mathbf{J}_{\text{sat}})\delta_s(\mathbf{r}), \qquad (7)$$

with

$$\mathbf{J}_{\text{lin}} = \sigma_{\text{nsat}}\mathbf{E}_{||}, \qquad (8a)$$

$$\mathbf{J}_{\text{sat}} = \sigma_{\text{sat}}(N_c)\mathbf{E}_{||}, \qquad (8b)$$

where $\mathbf{J}_{\text{lin}}$ is the linear surface current density and $\mathbf{J}_{\text{sat}}$ is the nonlinear current due to SA. The carrier density is also a function of time $N_c = N_c(\mathbf{E}, t)$ and Eq. (8b) would formally have to be a convolution between the conductivity and electric field, since it is written in the time domain. In order for Eq. (8b) to hold in its current form, the carrier lifetime has to be much longer than the time scale of current density generation. This means that the applied field interacts very fast (instantly) with the conductivity of the medium and generates the current density and photoexcited carriers, but the carriers themselves decay at a much longer (finite) time scale. In a two-level system configuration this is called the "rate-equation regime" where a separate equation is used to calculate the carrier density distribution [42]. In this work, assuming the above conditions hold, we use the following general relation for the carrier density,

$$\frac{\partial N_c}{\partial t} = \frac{\tfrac{1}{2}\text{Re}\{\sigma_{\text{sat}}(N_c)\}|\mathbf{E}_{||}|^2}{\hbar\omega_0} - \frac{N_c}{\tau} + D\nabla^2 N_c, \qquad (9)$$

where $\tfrac{1}{2}\text{Re}\{\sigma_{\text{sat}}(N_c)\}|\mathbf{E}_{||}|^2$ is the absorbed power density (W/m^2) corresponding to the saturable conductivity of the 2D material, τ is the SA relaxation time, and D the diffusion coefficient. Carrier diffusion exclusively takes place within the 2D material. Also, the Laplace operator is only applied in the transverse plane and not the propagation direction, that is, $\nabla^2 \equiv \nabla_t^2$. This can be justified under the slow varying amplitude approximation (SVEA): Assuming that the carrier density distribution follows that of the field, then under the SVEA condition second derivatives in the propagation direction can be neglected. Finally, note that Eq. (9) assumes that every absorbed photon has energy approximately equal to $\hbar\omega_0$ and it excites a single carrier.

By using the absorbed power density as the source term in Eq. (9) instead of the absorption coefficient and light intensity we don't make the assumption that saturation is uniform

across the material or that $\mathbf{E}_\parallel$ has a uniform spatial distribution. Consequently, N_c is calculated for each point on the 2D saturable absorber and thus can more accurately describe the SA phenomenon in situations where the electric field is highly nonuniform, which is especially true for nanophotonic waveguides.

B. Saturation of graphene conductivity

Graphene's linear surface conductivity is commonly attributed to interband and intraband electronic transitions which give rise to an interband and intraband surface current [43], respectively. Saturation of the absorption in graphene is directly linked to the saturation of these two currents and consequently the saturation of the associated conductivities. Expressions for the interband σ_{inter} and intraband σ_{intra} conductivities can be found in a number of published works [40]. Although both of these types of conductivities exhibit saturation with increasing field strength [39], intraband transitions at the near infrared spectral region (NIR) saturate at a much higher incident power density (GW/cm^2) compared to interband transitions (MW/cm^2). Also, in the NIR absorption is dominated by interband transitions. As a result, for applications in the NIR we can safely assume that the intraband conductivity is nonsaturable and we can attribute SA effects solely to interband transitions. In terms of Eq. (6) this translates to

$$\sigma_1(N_c) = \sigma_{\text{intra}} + \sigma_{\text{inter}}(N_c). \tag{10}$$

Furthermore, graphene's surface conductivity is also a function of the chemical potential (μ_c) at which graphene is biased. A plot of the real and imaginary parts of the conductivities σ_1, σ_{inter}, and σ_{intra} at 1550 nm, a temperature of 300 K, and for low intensities (linear regime) can be found in Fig. 1(a). For $\mu_c > \hbar\omega/2$ interband transitions are prohibited by Pauli blocking and so we expect that any SA effects in this region are caused by intraband saturation and in the NIR region will be relevant only at very high incident power densities that are beyond practical interest. On the other hand, for $\mu_c < \hbar\omega/2$, the interband conductivity is much larger than the intraband one and noticeable SA effects are expected, also at much lower power densities. Thus, we will study the SA of graphene for $\mu_c < \hbar\omega/2$, which for the telecom wavelength $\lambda_0 = 1.55\,\mu$m translates to $\mu_c < 0.4\,$eV. Note that for lower frequencies (e.g., the THz regime) interband transitions occur only for very small values of μ_c so that in general intraband transitions are the dominant component. Thus, in the THz regime graphene has to be accurately electrically biased or even self-biased very close to 0 eV [44,45] in order to exploit the saturation of interband transitions. Additionally, the saturation intensity of intraband transitions was reported in [39] to be proportional to λ^{-2} which means intraband transitions in the THz could possibly also be used for SA applications. As a result, the THz regime is also viable for graphene SA applications but because in those frequencies graphene can guide light by supporting surface plasmons, this regime will not be discussed in this work. According to the above, we plot in Fig. 1(b) the expected absorption modulation versus chemical potential for a graphene sheet illuminated by a homogeneous field (1550 nm) strong enough to fully saturate σ_{inter}. In this
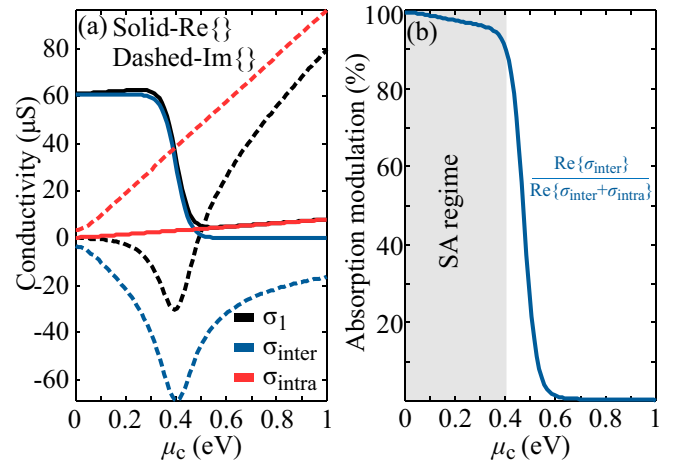

FIG. 1. All plots correspond to a free space wavelength of 1550 nm and a temperature of 300 K. (a) Graphene linear (at low incident power) conductivity σ_1 versus chemical potential. Also shown separately are the intraband σ_{intra} and interband σ_{inter} conductivities. Real and imaginary parts are depicted with solid and dashed lines, respectively. (b) Ideal absorption modulation of a graphene sheet under homogeneous illumination and for full saturation of σ_{inter}. Under these conditions the modulation is given by the conductivity ratio Re$\{\sigma_{\text{inter}}\}$/Re$\{\sigma_1\}$. The gray shaded area corresponds to the strong SA regime.

idealized scenario we observe that for $0\,$eV $< \mu_c < 0.4\,$eV the absorption modulation is between 100% and 90%.

Finally, graphene's surface interband conductivity is in general complex [see Fig. 1(a)] and according to Eq. (10) we expect that both the real and imaginary part are affected with increasing light intensity. The real part is saturated (decreased), which is the SA effect, but the imaginary part in graphene will actually increase (in magnitude) as was shown in [46]. This is nonlinear change in graphene's effective refractive index can possibly be important in applications sensitive to nonlinear phase change, such as resonators [47]. Moreover, recent publications [21,48] suggest that what was previously observed as the Kerr effect is actually the result of the modification of the imaginary part of the conductivity due to SA. In this work we will primarily focus on the saturation of absorption in straight waveguides and we choose to include the nonlinear phase change through the Kerr effect, which is better documented in the literature. Furthermore, we assume that graphene is pristine, e.g., $\mu_c = 0\,$eV, so that σ_{inter} is almost purely real. To simplify notation, from this point on when referencing to σ_{inter} we will implicitly refer to Re$\{\sigma_{\text{inter}}\}$.

The dependence of the absorption on the carrier density is estimated in [25] as $1/(1 + N_c/N_{\text{sat}})$ and more recently in [21,33] as $1 - N_c/(2N_{\text{sat}})$, where N_{sat} is the saturation density. We define N_{sat} as the steady-state carrier density at which the conductivity drops to one-half of its unsaturated value. Both of these approaches are phenomenological but provide a simple saturation function. We choose to adopt the expression from [21] which translates to

$$\sigma_{\text{inter}}(N_c) = \sigma_{\text{inter}}\left(1 - \frac{N_c}{2N_{\text{sat}}}\right), \tag{11}$$

where $\sigma_{\text{inter}} \equiv \sigma_{\text{inter}}(0)$ is thought to be the linear low-intensity value of the interband surface conductivity. According to Eq. (11) we can now express Eq. (8b) as

$$\mathbf{J}_{\text{sat}} = \sigma_{\text{inter}}\left(1 - \frac{N_c}{2N_{\text{sat}}}\right)\mathbf{E}_\parallel, \tag{12}$$

which is the SA nonlinear current from a 2D graphene sheet. We can also rewrite Eq. (9) using Eq. (11) as

$$\frac{\partial N_c}{\partial t} = \frac{\text{Re}\{\sigma_{\text{inter}}\}\left(1 - \frac{N_c}{2N_{\text{sat}}}\right)|\mathbf{E}_\parallel|^2}{2\hbar\omega_0} - \frac{N_c}{\tau} + D\nabla^2 N_c, \tag{13}$$

by using the Re{} notation here we underline the fact that even if we took into account the change of the imaginary part of σ_{inter} with the carrier density, Eq. (9) would still only depend on the real part.

It is useful to examine the case where we have continuous wave (cw) and homogeneous illumination at saturation conditions. By dropping the time derivative (steady state) and the dispersion term (homogeneous field) in Eq. (13), we can calculate the saturation carrier density by substituting $N_c = N_{\text{sat}}$,

$$N_{\text{sat}} = \frac{\text{Re}\{\sigma_{\text{inter}}\}Z_0 I_{\text{sat}}}{2\hbar\omega_0}\tau, \tag{14}$$

where Z_0 is the free space impedance and $I_{\text{sat}} = |E_{\parallel,\text{sat}}|^2/(2Z_0)$ is the saturation intensity. By using Eq. (14) in Eq. (13) we can also find the cw steady-state carrier density of a homogeneous field,

$$\frac{N_c}{N_{\text{sat}}} = \frac{2I/I_{\text{sat}}}{1 + I/I_{\text{sat}}}, \tag{15}$$

where we defined the intensity as $I = |\mathbf{E}_\parallel|^2/(2Z_0)$. It is now straightforward to show that substituting Eq. (15) into Eq. (11) leads to the well-known saturation expression,

$$\sigma_{\text{inter}}(I) = \frac{\sigma_{\text{inter}}}{1 + I/I_{\text{sat}}}. \tag{16}$$

From Eq. (16) it immediately follows that the nonlinear current density is

$$\mathbf{J}_{\text{sat}} = \frac{\sigma_{\text{inter}}}{1 + I/I_{\text{sat}}}\mathbf{E}_\parallel, \tag{17}$$

which describes SA in a straightforward way without the need for a rate equation in the case of homogeneous cw fields.

Last but not least, we discuss the values of the parameters N_{sat}, I_{sat}, and τ for graphene at 1550 nm. As the last two parameters are the ones that can be directly experimentally measured we focus on them and we estimate the value of N_{sat} from Eq. (14). In published experimental and theoretical results [24,26,34–39] the value of I_{sat} ranges from 1 MW/cm² to 1 GW/cm². Although experimental conditions and the specific setup (for example, the type of substrate that graphene is deposited on) will affect the measurement, it is very important to note that I_{sat} is by definition a cw intensity and thus measurements are accurate only for cw or long pulse excitation so that a steady state can be approximated. For the case of graphene, this translates into pulses in the ps-ns regime. Furthermore, the applied probe field must also be as homogeneous as possible. In structures with high field confinement, such as waveguides or microfibers, the carrier

TABLE I. Values of SA parameters used.

I_{sat}	τ	N_{sat}	D
1 MW/cm²	1.67 ps	1.5×10^{15} m⁻²	5500 cm²/s

spatial diffusion $D\nabla^2 N_c$ becomes important and can even be more significant than carrier relaxation [38]. Thus, the most accurate method of estimating I_{sat} would be a plane wave incident on a free standing graphene sheet. Following these observations, we adopt the value of $I_{\text{sat}} = 1$ MW/cm² which was reported in [25,38].

Continuing, the SA relaxation time τ in Eq. (13) for graphene represents an effective time which depends on two distinct time scales in graphene: The first one is the carrier-carrier intraband scattering (thermalization), reported in the range of 70–150 fs, and the second one is the carrier-phonon intraband scattering or electron-hole recombination (carrier cooling) in the range of 0.5–1.7 ps. These processes are explained in detail in [23] and were experimentally estimated in [49,50]. Note that the value of the effective parameter τ also depends on the specific setup as the carrier lifetime can be altered by a number of exterior factors. Reported estimated values of τ range from ultrafast values coinciding with the carrier thermalization process (50–150 fs) [33,39], some average of the thermalization and carrier cooling process (0.5–1 ps) [21,24,51], or the carrier cooling itself (1.67 ps) [25,38]. In the present work we opt for choosing $\tau = 1.67$ ps so that the estimated N_{sat} by Eq. (14) is similar to that used in [33]. A complete table with all the selected values can be found in Table I.

Finally, we would like to note that the choice of I_{sat} or τ_{sat} is not independent of each other, as can be seen in Eq. (14) when keeping N_{sat} constant, or by a more rigorous calculation in [39]. Qualitatively, this can be understood by the fact that if the photoexcited carrier density depletes faster then more power is needed to sustain the saturation effect.

III. NLSE FORMULATION

In this section we will derive the nonlinear parameters of the nonlinear Schrödinger equation (NLSE) that describes the wave propagation in waveguides with 2D saturable absorbers. For the sake of completeness we will consider both third-order and SA nonlinear phenomena. The analysis will be specialized for the case of two fields of the same waveguide mode but at distinct frequencies, which is often how SA experiments are conducted. The derivation of the NLSE is a well-known procedure [52,53] so it will not be fully expanded here but we note the fundamental restriction that should be satisfied: The effect of nonlinearity on the waveguide modes is thought as a small perturbation, that is, mode profiles do not change under nonlinear effects and propagation constants are only perturbed. This is almost always the case for Kerr effects but it is not obvious for SA where the conductivity of a material can be fully saturated. Nevertheless, in this work we will focus on SA from graphene in nanophotonic waveguides in the NIR spectral region. These waveguide modes are predominantly photonic in nature, which means that light is guided by the underlying waveguide structure and not graphene. Thus, the

presence of the graphene layers will not alter the guided mode's profile in any appreciable manner [54]. For such photonic waveguides we can safely assume that the NLSE restrictions hold.

We start by considering the real electric field $\mathcal{E}$ in a waveguide, which consists of a sum of all quasimonochromatic fields with distinct center frequencies ω_ν,

$$\mathcal{E}(\mathbf{r}, t) = \frac{1}{2}\left[\sum_\nu \mathbf{E}_\nu(\mathbf{r}, t) e^{-i\omega_\nu t} + \text{c.c.} \right], \qquad (18)$$

where $\mathbf{E}(\mathbf{r}, t)$ the complex electric field envelope, $\mathbf{r}$ the position vector, t the time, and

$$\mathbf{E}_\nu(\mathbf{r}, t) = A_\nu(z, t) \frac{\mathbf{e}_\nu(x, y, \omega_\nu)}{\sqrt{N_\nu}} e^{i\beta_0^{(\nu)} z}, \qquad (19)$$

where $\mathbf{e}_\nu(x, y, \omega_\nu)$ is the transverse mode profile at ω_ν, $\beta_0^{(\nu)} = \beta^{(\nu)}(\omega_\nu)$ the mode propagation constant, and

$$N_\nu = \frac{1}{2} \text{Re}\left\{ \iint \mathbf{e}_\nu \times \mathbf{h}_\nu^* \cdot \hat{\mathbf{z}}\, dS \right\} \qquad (20)$$

a normalization constant so that $|A_\nu|^2$ represents the mode's guided power. In Eq. (20) the integration is carried out over the waveguide's transverse cross section S. Note that A_ν contains the effect of both linear dispersion and nonlinear effects. In the frequency domain Eqs. (18) and (19) are

$$\text{FT}\{\mathcal{E}(\mathbf{r}, t)\} = \frac{1}{2}[\tilde{\mathbf{E}}(\mathbf{r}, \omega) + \tilde{\mathbf{E}}^*(\mathbf{r}, -\omega)], \qquad (21a)$$

$$\tilde{\mathbf{E}}(\mathbf{r}, \omega) = \sum_\nu \tilde{A}_\nu(z, \omega - \omega_\nu) \frac{\mathbf{e}_\nu(x, y, \omega_\nu)}{\sqrt{N_\nu}} e^{i\beta_0^{(\nu)} z}, \qquad (21b)$$

where $\text{FT}\{\cdot\}$ is the Fourier transform and we have chosen to distinguish frequency domain fields from time domain ones using the tilde notation.

The Kerr effect is most commonly introduced in Maxwell's equations through a nonlinear polarization term $\mathcal{P}_3$ for bulk materials and nonlinear surface current densities $\mathcal{J}_3$ for 2D materials [11]. If we also include the SA effect from 2D materials by using Eq. (8) we can write Maxwell's equations in the frequency domain as

$$\nabla \times \tilde{\mathbf{E}} = i\omega\mu_0 \tilde{\mathbf{H}}, \qquad (22a)$$

$$\nabla \times \tilde{\mathbf{H}} = -i\omega\varepsilon_0 \bar{\varepsilon}_r \tilde{\mathbf{E}} + \tilde{\mathbf{J}}_{\text{lin}} - i\omega\tilde{\mathbf{P}}_3 + \tilde{\mathbf{J}}_3 \delta_s(r) + \tilde{\mathbf{J}}_{\text{sat}}\delta_s(r), \qquad (22b)$$

where $\bar{\varepsilon}_r$ is the bulk relative dielectric permitivity tensor, $\tilde{\mathbf{P}}_3$ the frequency domain envelope of the third-order polarization, and $\tilde{\mathbf{J}}_3$ the frequency domain envelope of the third-order surface current density. The linear current density $\tilde{\mathbf{J}}_{\text{lin}}$ encompasses all of the linear current densities (bulk or 2D) present. The frequency domain envelopes are the Fourier transform of the respective time domain envelopes defined from the real fields as

$$\mathcal{P}_3(\mathbf{r}, t) = \frac{1}{2}\left[\sum_{\nu'} \mathbf{P}_{3,\nu'}(\mathbf{r}, t) e^{-i\omega_{\nu'} t} + \text{c.c.} \right], \qquad (23a)$$

$$\mathcal{J}_3(\mathbf{r}, t) = \frac{1}{2}\left[\sum_{\nu'} \mathbf{J}_{3,\nu'}(\mathbf{r}, t) e^{-i\omega_{\nu'} t} + \text{c.c.} \right], \qquad (23b)$$

$$\mathcal{J}_{\text{sat}}(\mathbf{r}, t) = \frac{1}{2}\left[\sum_{\nu'} \mathbf{J}_{\text{sat},\nu'}(\mathbf{r}, t) e^{-i\omega_{\nu'} t} + \text{c.c.} \right], \qquad (23c)$$

where ν' denotes all the possible frequency components that can be created through frequency-mixing nonlinear processes.

Following the standard derivation of the NLSE and using Eq. (22) for each distinct propagating frequency we can write the frequency domain equations of the slowly varying envelopes $\tilde{A}_\nu$ as

$$\frac{\partial}{\partial z}\tilde{A}_\nu(z, \omega - \omega_\nu) = i \sum_{n=1}^\infty \frac{(\omega - \omega_\nu)^n}{n!} \beta_n^{(\nu)} \tilde{A}_\nu(z, \omega - \omega_\nu)$$
$$+ \frac{i\omega e^{-i\beta_0^{(\nu)} z}}{4\sqrt{N_\nu}} \iint \mathbf{e}_\nu^* \cdot \left[\tilde{\mathbf{P}}_{3,\nu}(\mathbf{r}, \omega - \omega_\nu) \right.$$
$$+ \frac{i}{\omega}\tilde{\mathbf{J}}_{3,\nu}(\mathbf{r}, \omega - \omega_\nu)\delta_s(\mathbf{r})$$
$$\left. + \frac{i}{\omega}\tilde{\mathbf{J}}_{\text{sat},\nu}(\mathbf{r}, \omega - \omega_\nu)\delta_s(\mathbf{r}) \right]dS, \qquad (24)$$

where $\beta_n^{(\nu)}$ is the nth derivative of the propagation constant with respect to ω, calculated at ω_ν. The first term in the right-hand side stands for the linear dispersion while the terms in brackets account for third-order nonlinear effects and SA.

Equation (24) is now transformed back to the time domain as

$$\frac{\partial}{\partial z}A_\nu(z, t) = \sum_{n=1}^\infty \frac{i^{n+1}}{n!} \beta_n^{(\nu)} \frac{\partial^n}{\partial t^n}A_\nu(z, t)$$
$$+ \frac{i\omega_\nu}{4\sqrt{N_\nu}} e^{-i\beta_0^{(\nu)} z} \iint \mathbf{e}_\nu^* \cdot \mathbf{P}_{3,\nu}(\mathbf{r}, t)dS$$
$$- \frac{1}{4\sqrt{N_\nu}} e^{-i\beta_0^{(\nu)} z} \int \mathbf{e}_\nu^* \cdot \mathbf{J}_{3,\nu}(\mathbf{r}, t)d\ell$$
$$- \frac{1}{4\sqrt{N_\nu}} e^{-i\beta_0^{(\nu)} z} \int \mathbf{e}_\nu^* \cdot \mathbf{J}_{\text{sat},\nu}(\mathbf{r}, t)d\ell,$$
$$+ \frac{\alpha_\nu}{2}A_\nu, \qquad (25)$$

where the surface integrals regarding surface currents were transformed to line integrals, due to $\delta_s(\mathbf{r})$, on the respective 2D material. Furthermore, we have heuristically included the linear losses with $\alpha_\nu = 2\text{Im}\{n_{\text{eff}}^{(\nu)}\}k_0$, where $n_{\text{eff}}^{(\nu)}$ is the linear effective refractive index of the respective mode and k_0 the free space wave number. Note that nonsaturable losses induced by 2D materials are included in this parameter.

The next step is to find the time domain expressions for the nonlinear terms. To somewhat simplify the analysis we assume that there are only two fields propagating with $\nu = 1, 2$ corresponding to frequencies ω_1 and ω_2, respectively. Furthermore, the first field (pump) is assumed to be much stronger than the second one (probe) so that all nonlinear effects are attributed mainly to the first field. Also throughout this analysis the material response regarding $\mathbf{P}_3$ and $\mathbf{J}_3$ is taken to be instantaneous and we ignore any frequency mixing effects to other harmonics.

A. Third-order effects

The time domain expression for the third-order terms at ω_1 are

$$\mathbf{P}_{3,1} = \tfrac{3}{4}\varepsilon_0 \bar{\chi}^{(3)}(\omega_1; \omega_1, -\omega_1, \omega_1)|\mathbf{E}_1\mathbf{E}_1^*\mathbf{E}_1$$
$$+ \tfrac{3}{2}\varepsilon_0 \bar{\chi}^{(3)}(\omega_1; \omega_2, -\omega_2, \omega_1)|\mathbf{E}_2\mathbf{E}_2^*\mathbf{E}_1, \quad (26a)$$

$$\mathbf{J}_{3,1} = \tfrac{3}{4}\bar{\sigma}_s^{(3)}(\omega_1; \omega_1, -\omega_1, \omega_1)|\mathbf{E}_1\mathbf{E}_1^*\mathbf{E}_1$$
$$+ \tfrac{3}{2}\bar{\sigma}_s^{(3)}(\omega_1; \omega_2, -\omega_2, \omega_1)|\mathbf{E}_2\mathbf{E}_2^*\mathbf{E}_1, \quad (26b)$$

where the symbol $|$ denotes tensor multiplication, and the fourth rank tensors $\chi^{(3)}$ and $\sigma_s^{(3)}$ are the bulk third-order susceptibility and surface third-order conductivity, respectively. For isotropic nonlinear bulk and sheet materials the tensor elements are given by

$$\chi_{ijkl}^{(3)} = \tfrac{1}{3}\chi_3(\delta_{ij}\delta_{kl} + \delta_{ik}\delta_{jl} + \delta_{il}\delta_{jk}), \quad (27a)$$

$$\sigma_{s,ijkl}^{(3)} = \tfrac{1}{3}\sigma_3(\delta_{ij}\delta_{kl} + \delta_{ik}\delta_{jl} + \delta_{il}\delta_{jk}). \quad (27b)$$

In these expressions, $\{i, j, k, l\}$ refer to Cartesian components and δ_{pq} is the Kronecker delta. For the case of $\sigma_{s,ijkl}^{(3)}$ the indices correspond only to tangential to the 2D material components. The constants χ_3 and σ_3 are the only independent values of the respective tensors. We should note that the first terms in Eq. (26) represent self-phase modulation (SPM) while the second terms describe the cross-phase modulation (XPM). Furthermore, we underline that Eq. (26) contains only terms that are phase matched by default, irregardless of the specific propagation constants $\beta_0^{(1)}$, $\beta_0^{(2)}$ or frequencies ω_1, ω_2 chosen. By substituting Eq. (26) into Eq. (25) and removing the field amplitudes we can evaluate the nonlinear parameters from the respective integrals as

$$\gamma_{b,1} = \frac{\omega_1 \varepsilon_0}{16 N_1^2} \iint \chi_3 [2|\mathbf{e}_1|^4 + |\mathbf{e}_1^2|^2] dS, \quad (28a)$$

$$\gamma_{s,1} = \frac{-1}{16 N_1^2} \int \sigma_3 [2|\mathbf{e}_{1,\parallel}|^4 + |\mathbf{e}_{1,\parallel}^2|^2] d\ell, \quad (28b)$$

which are the SPM bulk and surface, respectively, nonlinear parameters of the field at ω_1 and

$$\gamma_{b,12} = \frac{\omega_1 \varepsilon_0}{8 N_1 N_2} \iint \chi_3 [|\mathbf{e}_1 \cdot \mathbf{e}_2^*|^2$$
$$+ |\mathbf{e}_1 \cdot \mathbf{e}_2|^2 + |\mathbf{e}_1|^2|\mathbf{e}_2|^2] dS, \quad (29a)$$

$$\gamma_{s,12} = \frac{-1}{8 N_1 N_2} \int \sigma_3 [|\mathbf{e}_{1,\parallel} \cdot \mathbf{e}_{2,\parallel}^*|^2$$
$$+ |\mathbf{e}_{1,\parallel} \cdot \mathbf{e}_{2,\parallel}|^2 + |\mathbf{e}_{1,\parallel}|^2|\mathbf{e}_{2,\parallel}|^2] d\ell, \quad (29b)$$

which are the XPM bulk and surface, respectively, nonlinear parameters for the cross phase modulation experienced by the field at ω_1 due to the field at ω_2. Notice that in $\gamma_{b,1}$ we did not include the imaginary unit i in the parameter, which will be later included in the complete NLSE equation. Regarding the second field at ω_2, the SPM contribution can be ignored since the field is considered weak and the XPM parameters are $\gamma_{b,21}/\omega_2 = \gamma_{b,12}/\omega_1$ and $\gamma_{s,21} = \gamma_{s,12}$.

B. Saturable absorption

We now move on to the SA term in Eq. (25). If the SA material is graphene then in the general case the SA nonlinear current is given by Eq. (12) which is complemented by the rate Eq. (13). For the case for cw fields and modes with low confinement one can also use Eq. (17) without a rate equation. Substituting the former, more general, expression into Eq. (25) we derive for the field at ω_1 that

$$-\frac{1}{4\sqrt{N_1}} e^{-i\beta_0^{(1)}z} \int \mathbf{e}_1^* \cdot \mathbf{J}_{\text{sat},1}(\mathbf{r}, t) d\ell$$
$$= -\frac{\sigma_{\text{inter}}}{4 N_1} \int \left(1 - \frac{N_c(x, y, t)}{2 N_{\text{sat}}}\right)|\mathbf{e}_{1,\parallel}(x, y)|^2 d\ell \; A_1(z, t), \quad (30)$$

from which we can extract the saturable nonlinear loss parameter,

$$\alpha_{\text{sat},1} = -\frac{\sigma_{\text{inter}}}{4 N_1} \int \left(1 - \frac{N_c(x, y, t)}{2 N_{\text{sat}}}\right)|\mathbf{e}_{1,\parallel}(x, y)|^2 d\ell. \quad (31)$$

The nonlinear loss parameter for the second field at ω_2 is found by changing index 1 to 2. We also underline that since we attribute the SA effect only to the first field, then in the rate Eq. (13) we can substitute $|\mathbf{E}_\parallel|^2 = |\mathbf{E}_{\parallel,1}|^2$ so that it leads to

$$\frac{\partial N_c}{\partial t} = \frac{\text{Re}\{\sigma_{\text{inter}}\}\left(1 - \frac{N_c}{2 N_{\text{sat}}}\right)|\mathbf{e}_{\parallel,1}|^2|A_1|^2}{2 N_1 \hbar \omega_1} - \frac{N_c}{\tau} + D\nabla^2 N_c. \quad (32)$$

Thus, the parameter $\alpha_{\text{sat},1}$ describes self-absorption modulation, that is the modulation of the absorption of field 1 by itself, while $\alpha_{\text{sat},2}$ describes cross absorption modulation, the modulation of the absorption of field 2 by the presence of field 1. We should also note that for graphene the strong field in frequency ω_1 will saturate losses for the field in ω_2 even if the two frequencies are not close to each other [55].

Finally, we combine all the nonlinear parameters into two coupled NLSE equations,

$$\frac{\partial}{\partial z} A_1 = \left(1/v_{\text{gm}} - 1/v_g^{(1)}\right)\frac{\partial}{\partial T}A_1 - i\frac{1}{2}\beta_2^{(1)}\frac{\partial^2}{\partial T^2}A_1$$
$$+ (i\gamma_{b,1} + \gamma_{s,1})|A_1|^2 A_1 + \alpha_{\text{sat},1} A_1 + \frac{\alpha_1}{2}A_1, \quad (33a)$$

$$\frac{\partial}{\partial z} A_2 = \left(1/v_{\text{gm}} - 1/v_g^{(2)}\right)\frac{\partial}{\partial T}A_2 - i\frac{1}{2}\beta_2^{(2)}\frac{\partial^2}{\partial T^2}A_2$$
$$+ (i\gamma_{b,21} + \gamma_{s,21})|A_1|^2 A_2 + \alpha_{\text{sat},2} A_2 + \frac{\alpha_2}{2}A_2, \quad (33b)$$

where we adopted a retarded time frame $T = t - z/v_{\text{gm}}$, $v_g^{(\nu)}$ is the group velocity of the νth field, $v_{\text{gm}} = (v_g^{(1)} + v_g^{(2)})/2$ the average group velocity, and we retained only the first two terms for the linear dispersion. It is also worth noting that Eqs. (31)–(33) can also be used to describe propagation in waveguides with few-layer graphene consisting of N_{gr} uncoupled monolayers. In this scenario both linear and nonlinear conductivities are multiplied by N_{gr} [except in Eq. (32)] and all the layers share the same saturation intensity and relaxation time [22].

To summarize, Eq. (33a) for the field at ω_1 contains the contributions from GVD, SPM, self-SA, and nonsaturable linear losses, while Eq. (33b) for the field at ω_2 contains
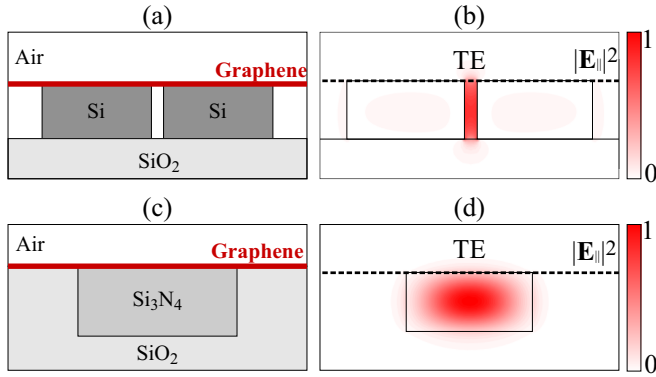
FIG. 2. Cross sections of a (a) silicon slot waveguide and (c) buried silicon nitride waveguide. On the top face of the waveguides a single monolayer graphene is deposited. (b) and (d) Normalized mode profiles of the field components parallel to the graphene sheet for the waveguide in (a) and (c), respectively. In (b) and (d) graphene is depicted with a dashed black line.

contributions from GVD, XPM, cross-SA, and nonsaturable linear losses. For the numerical solution of Eq. (33) we employ the Split-Step Fourier (SSF) method, where for each step dz we evaluate N_c from Eq. (32) assuming zero initial condition and taking the value of $|A_1|^2$ from the previous step. Then N_c is used to evaluate the nonlinear loss parameters which, together with the nonlinear parameters from the Kerr effect, is used to form the nonlinear operator for the SFF method.

IV. SIMULATION RESULTS

In this section we will first evaluate the SA nonlinear parameters assuming cw excitation and subsequently study pulsed excitation. For pulsed excitation we will also show when the Kerr effect becomes relevant and how this combined with linear dispersion can lead to quasisolitonic behavior. In all cases we assume that only the dominant TE polarized waveguide mode is excited. The waveguides that are going to be used can be seen in Figs. 2(a) and 2(c): First, a silicon slot waveguide on a silicon oxide substrate with dimensions 360 nm × 180 nm and a 40-nm gap. A graphene monolayer is deposited on top of the waveguide. In Fig. 2(b) we plot the norm of the electric field parallel to the graphene sheet, which in this case is $|\mathbf{E}_\parallel|^2 = |\mathbf{E}_x|^2 + |\mathbf{E}_z|^2$. The placement of graphene allows it to interact with the strongly confined field in the slot region of the waveguide. The other waveguide that we are going to use is the silicon nitride waveguide seen in Fig. 2(c), which was used in an experimental SA study [33]. The dimensions of the Si_3N_4 are 1500 nm × 600 nm and again a graphene monolayer is deposited on the top face of the waveguide, as seen in the schematic. In Fig. 2(d) we plot the norm of the field parallel to graphene. It can be seen that the field is a lot less confined and has a much smoother profile than the one of the slot waveguide.

A. cw excitation

In Fig. 3 we plot the SA nonlinear loss parameter (normalized to the zero power value of the saturable losses) versus the input average cw optical intensity evaluated as $|A|^2/A_{\text{eff}}$,
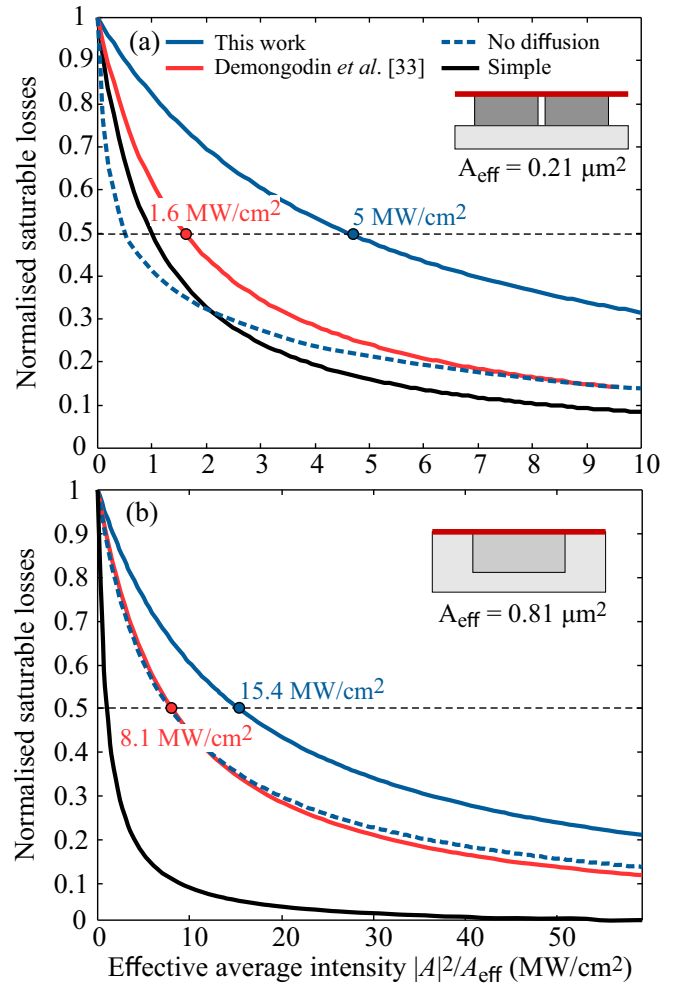

FIG. 3. Normalized saturable loss parameter versus average input cw intensity in the (a) silicon slot waveguide and (b) silicon nitride waveguide. Blue (dark gray) solid curves correspond to Eqs. (31) and (32) and red (light gray) curves to Eq. (34). The dashed blue (dark gray) curves are the same as the blue solid curves, but with carrier diffusion turned off ($D = 0$). The black curves serve as a reference for the case of a plain wave and are evaluated from Eq. (35). On the curves we note the effective saturation intensity predicted by each model. Insets show the respective waveguide cross section and the evaluated effective mode area.

where A is the complex field envelope [see Eq. (19)] of the guided mode and A_{eff} is the mode's effective field area [53]. We underline that we use the effective mode area so that results can be presented as average optical intensities, which is a more "native" quantity in the SA description. The actual guided power $|A|^2$ can be evaluated by multiplying values with A_{eff}.

We compare our results with a number of different SA models that are presented here. The solid blue (dark gray) curves are evaluated by Eqs. (31) and (32) taking into account the carrier diffusion term. The dashed blue (dark gray) curves are evaluated by the same equations but without the carrier diffusion term. This is equivalent to using Eq. (17) for the nonlinear saturable current. The red (light gray) curves are

evaluated through a model proposed in [33] which can be expressed through the following expressions:

$$\alpha_{\text{sat}} = \frac{\alpha_{\text{sat},0}}{2}(1 - N_c/2N_{\text{sat}}), \tag{34a}$$

$$\frac{\partial N_c}{\partial t} = \frac{\alpha_{\text{sat},0}(1 - N_c/2N_{\text{sat}})|A|^2}{\hbar\omega_0 W} - \frac{N_c}{\tau}, \tag{34b}$$

where $\alpha_{\text{sat},0}$ is the power loss coefficient associated with the saturable losses in the low (zero) intensity limit and W is the graphene length in the waveguide cross section. For the case of the silicon slot waveguide we considered $W = 760$ nm (two silicon wires plus the slot) and for the silicon nitride waveguide $W = 1500$ nm (full width of the silicon nitride). In the silicon slot waveguide, W was chosen to extend to the full width of the waveguide (and not just the slot area) so that we take into account the evanescent field and the E_z component guided in the silicon wires. Choosing a smaller W leads to an artificial enhancement of the source term in Eq. (34b). The black curve corresponds to the simplest possible SA model,

$$\alpha_{\text{sat}} = \frac{\alpha_{\text{sat},0}}{2}\frac{1}{1 + \dfrac{|A|^2}{A_{\text{eff}}I_{\text{sat}}}}, \tag{35}$$

which, by definition, saturates when $|A|^2/A_{\text{eff}}$ is equal to $I_{\text{sat}} = 1$ MW/cm^2. Physically, this last model would be accurate if the mode's profile was uniform and all of the guided power interacted with graphene, i.e., a plane wave illuminating an infinite free standing graphene sheet. This model serves as a point of reference to highlight how SA is differentiated in the respective contemporary waveguide.

We can draw several useful conclusions from Figs. 3(a) and 3(b). First of all, according to our approach we can evaluate the effective cw saturation intensity specific to a particular waveguide mode, which is 5 MW/cm^2 and 15.4 MW/cm^2 for the silicon slot and silicon nitride waveguide, respectively. The difference between the two values can be explained from the fact that in the silicon slot waveguide graphene is placed close to the maximum of the tightly confined field in the slot area and thus its losses can be saturated at lower power. On the other hand, in the silicon nitride waveguide graphene is placed on the top face which is very far from the center of the waveguide, where the field takes its maximum value.

Furthermore, the red (light gray) and blue (dark gray) curves predict different saturation intensities, with our results suggesting 2–5 times higher effective saturation intensities. It can be seen in Fig. 3(a) that both solid and dashed blue (dark gray) curves are distinct to the red (light gray) curves, implying that the differences of our model from that of [33] are not attributed just to the inclusion of the carrier diffusion term but also to the fact that we take into account the spatially dependent power density. Continuing, in Fig. 3(b) the dashed blue (dark gray) and red (light gray) curves are very close to each other, which means that in this case the difference between our approach [solid blue (dark gray)] and that of [33] [red (light gray) curve] is attributed solely to the inclusion of the carrier diffusion term. We believe that the agreement of the no-diffusion and [33] model is because $|A|^2/W$, that is used in Eq. (34b), is a much better approximation of the real power distribution over graphene in the case of the silicon

nitride waveguide than the slot waveguide. Nevertheless, it is interesting to note that even in low confinement waveguides carrier diffusion is still relevant and should be included in the SA modeling.

Finally, we discussed in Sec. II B that in experimental results the more homogeneous the field the better the I_{sat} approximation. At first, this seems to contradict our results as the silicon nitride waveguide deviates more from the nominal 1 MW/cm^2 than the silicon slot waveguide. The explanation lies with the fact that only a small portion of the guided field interacts with graphene and thus even though the mode profile is smooth on graphene a significant portion of the guided power is wasted.

B. Pulsed excitation

To demonstrate how a pulse propagates through the silicon slot waveguide with graphene we show two examples: a long [66-ps full width at half maximum (FWHM), 10-mW peak power] and a short (250-fs FWHM, 500-mW, or 1-W peak power) Gaussian pulse. The propagation length, defined in the linear (low power) regime as the length at which power drops by $1/e$, is calculated to be $L_{\text{prop}} = 18.4\ \mu$m. For the long pulse the group velocity dispersion and Kerr nonlinear length are $L_D = 163$ m and $L_{\text{NL}} = 10.4$ mm, respectively, while for the short pulse the same parameters were $L_D = 2.3$ mm and $L_{\text{NL}} = 208\ \mu$m or $L_{\text{NL}} = 104\ \mu$m when the peak power is 0.5 or 1 W, respectively. If the initial Gaussian pulse is of the form $A_{\text{in}} = \sqrt{P_0}\exp(-T^2/2T_0^2)$ then the above characteristic lengths are defined as

$$L_D = \frac{T_0^2}{\beta_2}, \tag{36a}$$

$$L_{\text{NL}} = \frac{1}{\gamma_s P_0}, \tag{36b}$$

where in our case $\gamma_s = -9600$ W^{-1}m^{-1} is the Kerr nonlinear parameter from graphene, since other contributions are negligible, and β_2 is the GVD parameter defined in Eq. (24). Specifically on the nonlinearity of the bulk materials, the nonlinear contribution of the Si areas was calculated to be $+45$ W^{-1}m^{-1} which is above two orders of magnitude lower than graphene's. The third-order graphene conductivity was taken to be $\sigma_3 = +i1.4 \times 10^{-21}$ Sm^2/V^2 which corresponds to defocusing behavior ($\gamma_s < 0$). The β_2 parameter was calculated to be 9.84 ps^2/m. Choosing the waveguide length equal to $L = 2L_{\text{prop}} \approx 40\ \mu$m we expect SA to be the dominant effect since for all cases $L \ll L_D, L_{\text{NL}}$.

The normalized output power of the long pulse is shown in Fig. 4(a) at different propagation distances. Solid curves represent the model developed in this work, taking into account both the finite relaxation time and carrier diffusion. On the other hand, dashed curves were calculated by ignoring the finite relaxation time [instant response, Eq. (16)]. Note though that the waveguide characteristics and carrier diffusion are still included by choosing the effective saturation intensity from the cw analysis presented in the previous section as $I_{\text{sat}} = 5$ MW/cm^2. The two models are almost identical and we can deduce that a simplified "instant" model suffices to simulated long pulse excitation but the saturation intensity has to be
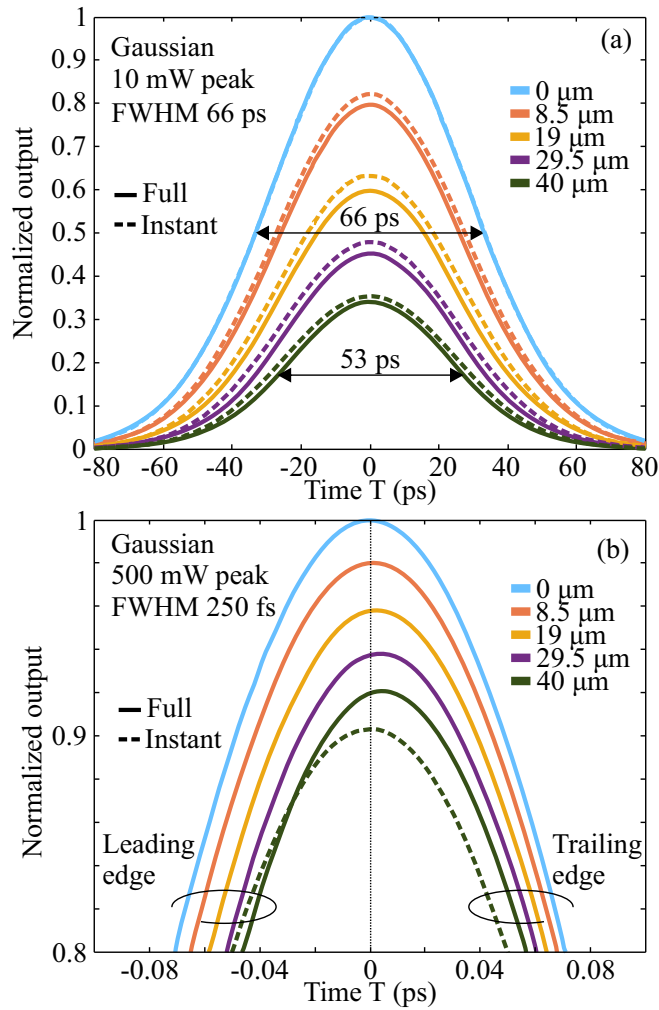
FIG. 4. Normalized output power versus time at various propagation distances of the silicon slot waveguide for a (a) long and (b) short pulse input. Solid curves correspond to the full model while dashed curves are evaluated as if SA was instantaneous or, equivalently, cw. In the latter case, we modified the saturation intensity to agree with the effective one calculated by the cw analysis, namely we set $I_{sat} = 5\,\mathrm{MW/cm^2}$. In (a) the two models are in agreement; there is noticeable pulse compression as the pulse propagates and the pulse deformation is symmetric. The FWHM of the pulses is noted with arrows on the curves. In (b) the leading edge of the pulse suffers greater losses than the trailing edge leading to asymmetric deformation and slight shifting of the pulse peak. These changes are not demonstrated by the dashed curves, which retain the symmetry.

modified according to the cw analysis. Considering the effects of SA, we can see that there is a ~20% temporal compression of the pulse, as the low power parts suffer much higher losses than the peak of the pulse. We underline that we chose a low peak power in order to demonstrate how effectively graphene SA can be used in compact silicon devices: Even for 10-mW peak power absorption is greatly saturated while the Kerr effect at this power level and propagation distance is negligible. Note though that for pulse compression applications since SA is an absorption-based effect some insertion losses should be expected. To this end, higher peak powers will lower propagation losses even further but will require higher propagation

distances to achieve the same pulse compression. Finally, we briefly discuss the effect of an increased relaxation time. According to Eq. (14) for the saturation carrier density N_{sat} of Table I and $\tau = 150\,\mathrm{fs}$, we evaluate $I_{sat} \approx 11\,\mathrm{MW/cm^2}$. Consequently, due to the increase of the saturation power the pulse of this example would experience only 11% temporal compression.

The short pulse propagation can be seen in Fig. 4(b). For clarity we have only drawn the final output pulse for the instant model (dashed curves). The solid curves now show a distinct asymmetric evolution of the pulse. Carriers begin accumulating at the leading edge of the pulse and because of their comparable to the pulse duration lifetime lead to lower absorption of the trailing edge. This also results into a slight shift in the position of the pulse peak. For higher propagation distances, this effect can become even more pronounced. On the other hand, the instant model discussed above cannot predict this kind of behavior. Furthermore, even though the 500-mW peak power is quite low for the duration of the pulse, it can be seen that absorption is heavily suppressed, as at 40 μm transmission is 0.9. On a final note, the 250-fs FWHM pulse is considered short with respect to the relaxation time τ of 1.67 ps considered; if the latter becomes comparable or even shorter than the pulse duration then asymmetry would become less pronounced and results would approach those of Fig. 4(a) but for higher peak powers and longer propagation distances, since decreasing τ would lead to an increase of I_{sat}.

In the previous example, for the given power level and propagation distance the Kerr effect was negligible. But because SA lowers absorption the Kerr effect will eventually manifest for higher propagation distances. To demonstrate this we use the above short pulse but with 1-W peak power and increase the propagation distance to 350 μm. The normalized spectral power density is shown in Fig. 5(a), where we observe that for propagation up to 170 μm the Kerr has little to no impact. But, at 260 μm and 350 μm we can spot the onset of the characteristic splitting of the peak at the central frequency due to the Kerr effect. The asymmetry in the spectrum is again the result of the finite SA relaxation time. What is more interesting is that in the time domain, shown in Fig. 5(b), we observe that when the Kerr effect becomes relevant the peak power of the pulse is increased and further temporal compression takes place. This rather unexpected increase of the peak power can be intuitively understood by noting that due to SA the pulse duration is decreased, which according to Eq. (36a), lowers the dispersion length. On the other hand the nonlinear length L_{NL} of Eq. (36b) is also lowered by the increase of the peak power but at a significantly lower rate. As a result, L_D approaches L_{NL} and we have confirmed that around 400 μm propagation distance $L_D \approx L_{NL}$, which is a known condition for the formation of a quasisoliton. Note that this phenomenon is only possible due to the defocusing Kerr nonlinearity of graphene ($\gamma_s < 0$) combined with the normal linear dispersion ($\beta_2 > 0$): By artificially reversing the sign of the Kerr nonlinearty the peak power increase vanishes.

Finally, to further explore possible applications of graphene SA in photonic waveguides we present in Fig. 6 the simultaneous propagation of two channels at wavelengths $\lambda_1 = 1549.6$ nm and $\lambda_2 = 1550.4$ nm. Results are evaluated by solving the coupled partial derivative system of Eq. (33). In

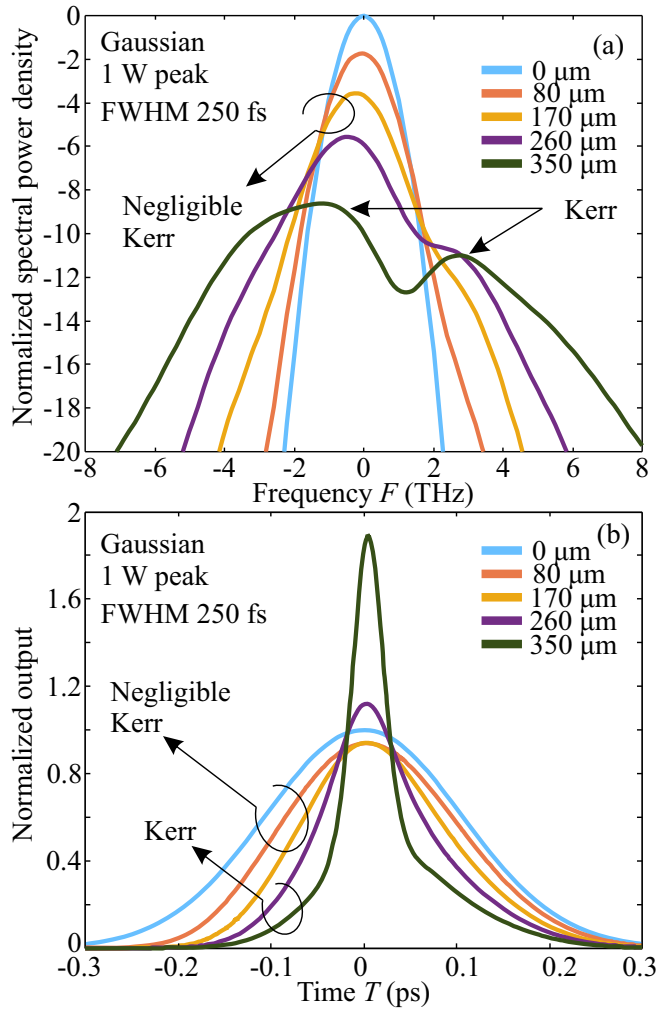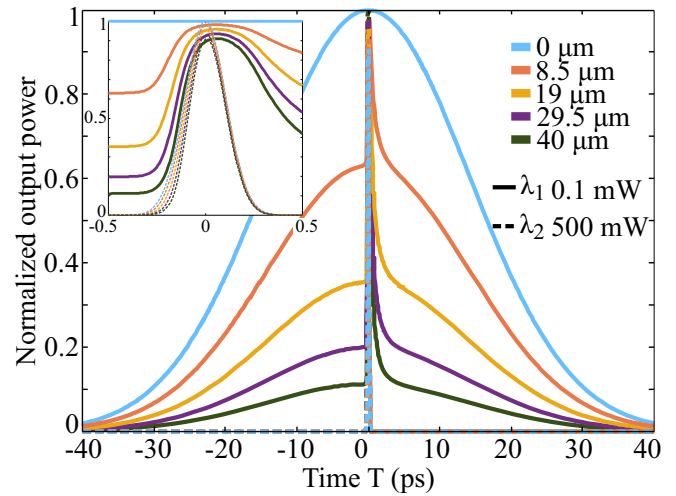FIG. 6. Normalized output power at different propagation distances for the scenario of simultaneous propagation of two pulses at different wavelengths in the silicon slot waveguide. Solid curves correspond to the weak long pulse at λ_1 while dashed curves to the high-power short pulse at λ_2. As the pulses propagate, the long pulse experiences cross absorption modulation from the short pulse at the region where temporal overlap exists. (inset) Zoom in around the short pulse to highlight the asymmetric temporal shaping of the long pulse, which is a direct consequence of the finite SA relaxation time. As a consequence of cross absorption modulation the short pulse is imprinted onto the λ_1 channel.

FIG. 5. (a) Spectra of the initial pulse at various propagation distances. For up to $170\,\mu$m there is little Kerr contribution and SA is the dominant effect. At $260\,\mu$m and $350\,\mu$m the Kerr effect becomes evident due to the formation of the two peaks. (b) Temporal evolution of the pulse at the same propagation distances. When the Kerr effect becomes strong we observe that the interplay between SA, the Kerr effect, and linear dispersion leads to the increase of the pulse peak and further temporal compression. Specifically, the decrease of the pulse duration lowers the dispersion length L_{D} which slowly approaches the nonlinear length L_{NL} and thus solitonic regime. This phenomenon is possible due to the defocusing character of graphene's Kerr nonlinearity ($\gamma_s < 0$) and normal dispersion regime ($\beta_2 > 0$).

the first channel propagates a weak long Gaussian pulse (33-ps FWHM, 0.1-mW peak power) and in the second channel a high power short Gaussian pulse (250-fs FWHM, 500-mW peak power). Note that the weak signal could also be cw and that only the second wavelength is responsible for the saturation of absorption. It can be seen that the high power pulse in the second channel is gradually imprinted to the first channel. Zooming in (inset), the asymmetric evolution of the weak pulse due to the finite carrier life time is evident and the resulting pulse is no longer Gaussian. The final FWHM pulse duration for the weak pulse at λ_1 is found to be around 0.61 ps which is a considerable reduction since the initial value was

33 ps. This example highlights a completely passive and compact way to duplicate data streams between optical channels. The restriction is that the configuration only works between high power and low power signals.

V. CONCLUSIONS

The main focus of this work was to present a solid theoretical framework to model propagation of light under the effect of SA in waveguides with graphene, together with the usual third-order nonlinear effects. We have discussed how experimental data should be introduced into the model and shown the importance of including the carrier diffusion term for high confinement waveguides. Under these conditions we have demonstrated that through a cw analysis we can extract an effective saturation intensity value (applicable to the specific guided mode) which can then in turn be used for a simplified approximation of the propagation of ps-long pulses. For pulses in the sub-ps regime though, the full model including the finite SA relaxation time and the carrier diffusion term, must be used to fully capture the temporal evolution under SA. The resulting power threshold for SA is very low compared to other nonlinear effects, such as the Kerr effect. Nevertheless, the combined effect of SA, the Kerr effect, and linear dispersion can further enhance the SA pulse compression. Finally, we have proposed a concept scheme for duplicating data streams between optical channels in integrated photonic waveguides.

[1] K. S. Novoselov, V. I. Fal′ko, L. Colombo, P. R. Gellert, M. G. Schwab, and K. Kim, A roadmap for graphene, Nature (London) **490**, 192 (2012).

[2] A. H. Castro Neto, F. Guinea, N. M. R. Peres, K. S. Novoselov, and A. K. Geim, The electronic properties of graphene, Rev. Mod. Phys. **81**, 109 (2009).

[3] P. Avouris, Graphene: Electronic and photonic properties and devices, Nano Lett. **10**, 4285 (2010).

[4] F. Wang, Y. Zhang, C. Tian, C. Girit, A. Zettl, M. Crommie, and Y. R. Shen, Gate-variable optical transitions in graphene, Science **320**, 206 (2008).

[5] M. Liu, X. Yin, E. Ulin-Avila, B. Geng, T. Zentgraf, L. Ju, F. Wang, and X. Zhang, A graphene-based broadband optical modulator, Nature (London) **474**, 64 (2011).

[6] I. Datta, C. T. Phare, A. Dutt, A. Mohanty, and M. Lipson, Integrated graphene electro-optic phase modulator, in *Conference on Lasers and Electro-Optics* (OSA, Washington, DC, 2017).

[7] F. Bonaccorso, Z. Sun, T. Hasan, and A. C. Ferrari, Graphene photonics and optoelectronics, Nat. Photonics **4**, 611 (2010).

[8] Q. Bao and K. P. Loh, Graphene photonics, plasmonics, and broadband optoelectronic devices, ACS Nano **6**, 3677 (2012).

[9] Z. Sun, A. Martinez, and F. Wang, Optical modulators with 2d layered materials, Nat. Photonics **10**, 227 (2016).

[10] S. A. Mikhailov, Non-linear electromagnetic response of graphene, Europhys. Lett. (EPL) **79**, 27002 (2007).

[11] E. Hendry, P. J. Hale, J. Moger, A. K. Savchenko, and S. A. Mikhailov, Coherent Nonlinear Optical Response Of Graphene, Phys. Rev. Lett. **105**, 097401 (2010).

[12] G. Demetriou, H. T. Bookey, F. Biancalana, E. Abraham, Y. Wang, W. Ji, and A. K. Kar, Nonlinear optical properties of multilayer graphene in the infrared, Opt. Express **24**, 13033 (2016).

[13] E. Dremetsika, B. Dlubak, S.-P. Gorza, C. Ciret, M.-B. Martin, S. Hofmann, P. Seneor, D. Dolfi, S. Massar, P. Emplit, and P. Kockaert, Measuring the nonlinear refractive index of graphene using the optical kerr effect method, Opt. Lett. **41**, 3281 (2016).

[14] S. A. Mikhailov, Nonperturbative quasiclassical theory of the nonlinear electrodynamic response of graphene, Phys. Rev. B **95**, 085432 (2017).

[15] N. A. Savostianova and S. A. Mikhailov, Optical Kerr effect in graphene: Theoretical analysis of the optical heterodyne detection technique, Phys. Rev. B **97**, 165424 (2018).

[16] T. Gu, N. Petrone, J. F. McMillan, A. van der Zande, M. Yu, G. Q. Lo, D. L. Kwong, J. Hone, and C. W. Wong, Regenerative oscillation and four-wave mixing in graphene optoelectronics, Nat. Photonics **6**, 554 (2012).

[17] D. A. Smirnova, A. V. Gorbach, I. V. Iorsh, I. V. Shadrivov, and Y. S. Kivshar, Nonlinear switching with a graphene coupler, Phys. Rev. B **88**, 045443 (2013).

[18] N. Kumar, J. Kumar, C. Gerstenkorn, R. Wang, H.-Y. Chiu, A. L. Smirl, and H. Zhao, Third harmonic generation in graphene and few-layer graphite films, Phys. Rev. B **87**, 121406(R) (2013).

[19] N. Vermeulen, D. Castelló-Lurbe, J. L. Cheng, I. Pasternak, A. Krajewska, T. Ciuk, W. Strupinski, H. Thienpont, and J. Van Erps, Negative Kerr Nonlinearity Of Graphene As Seen Via Chirped-Pulse-Pumped Self-Phase Modulation, Phys. Rev. Applied **6**, 044006 (2016).

[20] N. Vermeulen, J. Cheng, J. E. Sipe, and H. Thienpont, Opportunities for wideband wavelength conversion in foundry-compatible silicon waveguides covered with graphene, IEEE J. Sel. Top. Quantum Electron. **22**, 347 (2016).

[21] N. Vermeulen, D. Castelló-Lurbe, M. Khoder, I. Pasternak, A. Krajewska, T. Ciuk, W. Strupinski, J. Cheng, H. Thienpont, and J. V. Erps, Graphene's nonlinear-optical physics revealed through exponentially growing self-phase modulation, Nat. Commun. **9**, 2675 (2018).

[22] G. Xing, H. Guo, X. Zhang, T. C. Sum, and C. H. A. Huan, The physics of ultrafast saturable absorption in graphene, Opt. Express **18**, 4564 (2010).

[23] E. Malic, T. Winzer, E. Bobkin, and A. Knorr, Microscopic theory of absorption and ultrafast many-particle kinetics in graphene, Phys. Rev. B **84**, 205406 (2011).

[24] A. Malouf, O. Henderson-Sapir, S. Set, S. Yamashita, and D. J. Ottaway, Two-photon absorption and saturable absorption of mid-IR in graphene, Appl. Phys. Lett. **114**, 091111 (2019).

[25] Q. Bao, H. Zhang, Y. Wang, Z. Ni, Y. Yan, Z. X. Shen, K. P. Loh, and D. Y. Tang, Atomic-layer graphene as a saturable absorber for ultrafast pulsed lasers, Adv. Funct. Mater. **19**, 3077 (2009).

[26] Z. Sun, T. Hasan, F. Torrisi, D. Popa, G. Privitera, F. Wang, F. Bonaccorso, D. M. Basko, and A. C. Ferrari, Graphene mode-locked ultrafast laser, ACS Nano **4**, 803 (2010).

[27] Q. Sheng, M. Feng, W. Xin, T. Han, Y. Liu, Z. Liu, and J. Tian, Actively manipulation of operation states in passively pulsed fiber lasers by using graphene saturable absorber on microfiber, Opt. Express **21**, 14859 (2013).

[28] A.-P. Luo, P.-F. Zhu, H. Liu, X.-W. Zheng, N. Zhao, M. Liu, H. Cui, Z.-C. Luo, and W.-C. Xu, Microfiber-based, highly nonlinear graphene saturable absorber for formation of versatile structural soliton molecules in a fiber laser, Opt. Express **22**, 27019 (2014).

[29] X. M. Liu, H. R. Yang, Y. D. Cui, G. W. Chen, Y. Yang, X. Q. Wu, X. K. Yao, D. D. Han, X. X. Han, C. Zeng, J. Guo, W. L. Li, G. Cheng, and L. M. Tong, Graphene-clad microfibre saturable absorber for ultrafast fibre lasers, Sci. Rep. **6**, 26024 (2016).

[30] J. D. Zapata, D. Steinberg, L. A. M. Saito, R. E. P. de Oliveira, A. M. Cárdenas, and E. A. T. de Souza, Efficient graphene saturable absorbers on d-shaped optical fiber for ultrashort pulse generation, Sci. Rep. **6**, 20644 (2016).

[31] H. Li, Y. Anugrah, S. J. Koester, and M. Li, Optical absorption in graphene integrated on silicon waveguides, Appl. Phys. Lett. **101**, 111110 (2012).

[32] J. Wang, L. Zhang, Y. Chen, Y. Geng, X. Hong, X. Li, and Z. Cheng, Saturable absorption in graphene-on-waveguide devices, Appl. Phys. Express **12**, 032003 (2019).

[33] P. Demongodin, H. E. Dirani, J. Lhuillier, R. Crochemore, M. Kemiche, T. Wood, S. Callard, P. Rojo-Romeo, C. Sciancalepore, C. Grillet, and C. Monat, Ultrafast saturable absorption dynamics in hybrid graphene/Si_3N_4 waveguides, APL Photonics **4**, 076102 (2019).

[34] W. D. Tan, C. Y. Su, R. J. Knize, G. Q. Xie, L. J. Li, and D. Y. Tang, Mode locking of ceramic Nd:yttrium aluminum garnet with graphene as a saturable absorber, Appl. Phys. Lett. **96**, 031106 (2010).

[35] P. L. Huang, S.-C. Lin, C.-Y. Yeh, H.-H. Kuo, S.-H. Huang, G.-R. Lin, L.-J. Li, C.-Y. Su, and W.-H. Cheng, Stable mode-locked fiber laser based on CVD fabricated graphene saturable absorber, Opt. Express **20**, 2460 (2012).

[36] C.-C. Lee, J. M. Miller, and T. R. Schibli, Doping-induced changes in the saturable absorption of monolayer graphene, Appl. Phys. B **108**, 129 (2012).

[37] Z. Zheng, C. Zhao, S. Lu, Y. Chen, Y. Li, H. Zhang, and S. Wen, Microwave and optical saturable absorption in graphene, Opt. Express **20**, 23201 (2012).

[38] F. Zhang, S. Han, Y. Liu, Z. Wang, and X. Xu, Dependence of the saturable absorption of graphene upon excitation photon energy, Appl. Phys. Lett. **106**, 091102 (2015).

[39] A. Marini, J. D. Cox, and F. J. García de Abajo, Theory of graphene saturable absorption, Phys. Rev. B **95**, 125408 (2017).

[40] D. Chatzidimitriou, A. Pitilakis, and E. E. Kriezis, Rigorous calculation of nonlinear parameters in graphene-comprising waveguides, J. Appl. Phys. **118**, 023105 (2015).

[41] R. N. Zitter, Saturated optical absorption through band filling in semiconductors, Appl. Phys. Lett. **14**, 73 (1969).

[42] P. Butcher and D. Cotter, *The Elements of Nonlinear Optics*, Cambridge Studies in Modern Optics (Cambridge University Press, Cambridge, 1990).

[43] L. A. Falkovsky, Optical properties of graphene, J. Phys.: Conf. Ser. **129**, 012004 (2008).

[44] J. S. Gomez-Diaz, C. Moldovan, S. Capdevila, J. Romeu, L. S. Bernard, A. Magrez, A. M. Ionescu, and J. Perruisseau-Carrier, Self-biased reconfigurable graphene stacks for terahertz plasmonics, Nat. Commun. **6**, 6334 (2015).

[45] D. Correas-Serrano, A. Alù, and J. S. Gomez-Diaz, Magnetic-free nonreciprocal photonic platform based on time-modulated graphene capacitors, Phys. Rev. B **98**, 165428 (2018).

[46] A. Marini and F. J. Garcia de Abajo, Graphene-Based Active Random Metamaterials For Cavity-Free Lasing, Phys. Rev. Lett. **116**, 217401 (2016).

[47] V. G. Ataloglou, T. Christopoulos, and E. E. Kriezis, Nonlinear coupled-mode-theory framework for graphene-induced saturable absorption in nanophotonic resonant structures, Phys. Rev. A **97**, 063836 (2018).

[48] D. Castelló-Lurbe, H. Thienpont, and N. Vermeulen, Predicting graphene's nonlinear-optical refractive response for propagating pulses, Laser Photonics Rev. **14**, 1900402 (2020).

[49] M. Breusing, S. Kuehn, T. Winzer, E. Malić, F. Milde, N. Severin, J. P. Rabe, C. Ropers, A. Knorr, and T. Elsaesser, Ultrafast nonequilibrium carrier dynamics in a single graphene layer, Phys. Rev. B **83**, 153410 (2011).

[50] J. M. Dawlaty, S. Shivaraman, M. Chandrashekhar, F. Rana, and M. G. Spencer, Measurement of ultrafast carrier dynamics in epitaxial graphene, Appl. Phys. Lett. **92**, 042116 (2008).

[51] H. G. Rosa, J. A. Castañeda, C. H. B. Cruz, L. A. Padilha, J. C. V. Gomes, E. A. T. de Souza, and H. L. Fragnito, Controlled stacking of graphene monolayer saturable absorbers for ultrashort pulse generation in erbium-doped fiber lasers, Opt. Mater. Express **7**, 2528 (2017).

[52] A. Pitilakis, D. Chatzidimitriou, and E. E. Kriezis, Theoretical and numerical modeling of linear and nonlinear propagation in graphene waveguides, Opt. Quantum Electron. **48**, 243 (2016).

[53] S. A. V. and T. M. Monro, A full vectorial model for pulse propagation in emerging waveguides with subwavelength structures part i: Kerr nonlinearity, Opt. Express **17**, 2298 (2009).

[54] A. V. Gorbach and E. Ivanov, Perturbation theory for graphene-integrated waveguides: Cubic nonlinearity and third-harmonic generation, Phys. Rev. A **94**, 013811 (2016).

[55] Y. Y. Ren, M. Feng, K. Zhang, J. Yang, Y. Miao, F. F. Song, Z. B. Liu, and F. Song, Dual-wavelength cross absorption modulation theory based on graphene, Phys. Scr. **94**, 125506 (2019).